

Nanoscale

Accepted Manuscript



This is an *Accepted Manuscript*, which has been through the Royal Society of Chemistry peer review process and has been accepted for publication.

Accepted Manuscripts are published online shortly after acceptance, before technical editing, formatting and proof reading. Using this free service, authors can make their results available to the community, in citable form, before we publish the edited article. We will replace this *Accepted Manuscript* with the edited and formatted *Advance Article* as soon as it is available.

You can find more information about *Accepted Manuscripts* in the [Information for Authors](#).

Please note that technical editing may introduce minor changes to the text and/or graphics, which may alter content. The journal's standard [Terms & Conditions](#) and the [Ethical guidelines](#) still apply. In no event shall the Royal Society of Chemistry be held responsible for any errors or omissions in this *Accepted Manuscript* or any consequences arising from the use of any information it contains.

ARTICLE

Fe₃O₄ Nanoparticles Prepared by Seeded-Growth Route for Hyperthermia: Electron Magnetic Resonance as a Key Tool to Evaluate Size Distribution in Magnetic Nanoparticles.

Cite this: DOI: 10.1039/x0xx00000x

Received 00th January 2012,
Accepted 00th January 2012

DOI: 10.1039/x0xx00000x

www.rsc.org/

Idoia Castellanos-Rubio^a, Maite Insausti^{ab}, Eneko Garaio^c, Izaskun Gil de Muro^a, Fernando Plazaola^c, Teófilo Rojo^a, Luis Lezama^{*ab}

Monodispersed Fe₃O₄ nanoparticles have been synthesized by a thermal decomposition method based on seeded-growth technique, achieving size tunable nanoparticles with high crystallinity and high saturation magnetization. EMR spectroscopy becomes a very efficient complementary tool to determinate the fine details of size distributions of MNPs and even to estimate directly the size in a system composed of a given type of magnetic nanoparticles. The size and size dispersity affects directly to the efficiency of MNPs for hyperthermia and EMR provides a direct evaluation of these characteristics almost exactly in the same preparation and with the same concentration as used in hyperthermia experiments. The correlation observed between the Specific Absorption Rate (SAR) and the effective gyromagnetic factor (g_{eff}) is extremely remarkable and renders a way to assess directly the heating capacity of a MNP system.

Introduction

Magnetite (Fe₃O₄) nanoparticles arouse enormous interest for some biomedical applications as they combine useful magnetic properties, good biocompatibility and low cytotoxicity^{1,2}. Examples of potential use of these nanoparticles include topics as magnetic targeting, drug delivery, magnetic resonance imaging or, in particular, hyperthermia³⁻⁶, which makes use of the heating ability of magnetic nanoparticles (MNPs) under a radio frequency magnetic field. As a rule in these applications, particle size lies preferably below the superparamagnetic limit, preventing unwanted aggregation effects that could degrade the colloidal stability⁷. The performance of the MNPs in hyperthermia is usually measured through the so-called Specific Absorption Rate (SAR) which, apart from the particular characteristics of the applied AC magnetic field, depends on a number of critical properties of MNPs, as saturation magnetization, magnetic anisotropy, size, or colloidal stability^{8,9}. From the experimental point of view the way to find the best compromise of all is constrained by the ability to produce custom design MNPs of high quality, and this is still a major challenge nowadays. For this task the choice of an enough versatile and robust preparation method is decisive and wet chemical routes based on the thermal decomposition of organometallic precursors have proved to be very promising¹⁰⁻

¹², though water-solubility has to be achieved in a subsequent surface treatment¹³. Among the existing protocols of this preparation route, the seeded-growth method allows for a fine-tuning of particle size and yields monodisperse nanoparticles¹⁴. Although the seeded-growth method is well developed for 5d noble metal and II-VI semiconductor NPs, this process in 3d transition metals is much more challenging due to the difficulty to separate the nucleation and growth processes¹⁵. To accomplish this, the use of an appropriate mixture of surfactants¹⁶ is essential to ensure a homogenous growth of starting nuclei, avoiding aggregation of particles and improving colloidal stability¹⁷.

Seed mediated growth has been little used in previous works to produce MNPs for hyperthermia, especially if it is compared to other wet synthetic routes, which lead often to more polydisperse materials. Recently, Guardia et al. reported high values of SAR in cube-shape nanocrystals with edge lengths from 12(±1) to 38(±9) nm prepared by thermal decomposition method, but the hypothetical correlation between MNPs size and SAR values was not observed¹⁸. Formerly, Levy et al were able to control finely the size of magnetite nanoparticles by using a one-pot seeded-growth method¹⁹, but SAR and magnetic properties were found to be worse than expected. The existence of strong surface effects and/or frustrated magnetic layer was postulated as a possible

explanation of the unexpectedly low magnetization in the initial seeds, which became even lower for larger particles.

In this synthetic method, successive additions of reagents over previously synthesized magnetic particles promotes to some extent the formation of several populations of magnetic cores with distinct sizes coexisting in the same sample; especially when seeded-growth is carried out in a multi-pot method, namely, when additions are done in independent reaction vessels, using previously isolated product as a seed. This effect, more significant in the growing of larger nanoparticles, often requires additional cleaning processes of the as-prepared samples to hit good monodispersity. In this way, the success of the seeded-growth requires the ability to confirm the high quality of seeds and to detect subtle changes in size distributions of magnetic cores. For this purpose, those techniques specifically sensitive to magnetic properties come to be an essential instrument and help to understand why magnetic response of samples is sometimes so far away from the expected one.

In this sense, the use of a sensitive tool, as Electron Magnetic Resonance (EMR), largely amplifies the ability to detect small changes in any system of magnetic nanoparticles. EMR can provide useful information on particle size evaluation, shape and surface effects or inter-particle interactions^{20,21}. By the use of a correct strategy to eliminate the influence of sample handling over the reproducibility of experiments, EMR can be exploited in the study of MNPs^{22,23}. For the particular case of magnetite nanoparticles, the room temperature EMR spectra measured on solid samples show asymmetric lines with rather large line-widths, rapidly increasing with particle size. In addition, resonance fields depend on the amount of powder and small angular dependences of resonant line positions have been observed even in apparently totally disordered systems. Most of these problems can be minimized when the spectra are recorded in a colloidal medium, as toluene dispersions. For this reason, all the EMR measurements presented in this work have been carried out directly in liquid samples, so that all the spectra are reproducible.

To sum up, EMR technique is proposed as a complementary tool to Transmission Electron Microscopy (TEM) to evaluate the size distribution of the whole sample of magnetite nanoparticles used in hyperthermia measurements. The impact of size and dispersion in the performance of MNPs for hyperthermia is still a matter of debate and direct comparison of EMR and SAR measurements will provide evidences in this sense. In this work, the seeded-growth method has been shown as a very suitable synthetic route to adjust the size and monodispersity of oleic acid coated Fe₃O₄ NPs with high magnetization values. The so-obtained samples, that exhibit strong size-dependent heating power, well compatible with the theory, could have a promising applicability in hyperthermia therapies.

Experimental

Materials

Iron (0) pentacarbonyl, 1,2-hexadecanediol (90%), oleic acid (98%), oleylamine (70%), benzyl ether (99%) and toluene (99.8%) were purchased from Sigma-Aldrich and used as received without purification. Ethanol was purchased from Panreac S.A

Synthetic procedure

Fe₃O₄ nanoparticles with diameters from 4.3 to 14.9 nm (samples A-F) have been prepared by a modified solution-phase thermal decomposition method²⁴. The innovation is based on seed mediated growth²⁵ and the subsequent purifying process monitorized by EMR. High homogeneity is achieved when 3 types of ligands with different affinity for iron atoms (carboxylic acid, alcohol and amine, from higher to smaller affinity) are combined in a specific molar ratio. In a typical synthesis of 4 nm Fe₃O₄ nanoparticles (sample A), benzyl ether (20 ml), oleic acid (1 mmol), 1,2-hexadecanediol (20 mmol) and oleylamine (6 mmol) were mixed and mechanically stirred under Ar flow. The mixture was heated to 140 °C and then Fe(CO)₅ (0.75 mmol) was added under a blanket of Argon. Finally, the mixture was heated to reflux (298 °C) for 30 min, resulting in black solution. No specific oxidation step such as air exposure or chemical oxidation was carried out²⁶⁻²⁸, but the synthesis was not made in completely free oxygen conditions, and small concentration of O₂ or H₂O would be expected in the reaction vessel, coming from the air and/or reagents and solvents used without further purification. The little oxygen supply could be enough to oxidize Fe(0) gradually and to form a thermodynamically stable magnetite phase. The black mixture was cooled down to room temperature by removing the heat source. After addition of ethanol and centrifugation at 4000 rpm for 4 hours, the monodisperse 4 nm Fe₃O₄ nanoparticles were obtained. Samples B, D and E were synthesized by the seeded-growth technique with 3, 4 and 5 consecutive additions of Fe(CO)₅ and ligands, respectively, in the same reaction vessel, which corresponds to one-pot method. In contrast, sample C was synthesized in a two-pot procedure by injecting iron precursor and surfactants (oleic acid, 1,2-hexadecanediol and oleylamine) on sample B. In all the cases the amount of iron precursor and ligands added in each step was calculated taking into account the desired size of the nanoparticles (Table S1, S.I.). It has been noticed that the reactive concentration is an important synthetic parameter in the particle growth. Thus, sample F was also obtained by 5 consecutive additions, but the concentration of the reagents was reduced to half, leading to smaller NPs, as expected. Several washing cycles with toluene and ethanol were carried out in order to obtain highly monodisperse samples.

Characterization

Iron content of samples was determined by Inductively Coupled Plasma-Atomic Emission Spectroscopy (ICP-AES) using an ELAN 9000 ICP-MS (Perkin-Elmer SCIEX) spectrophotometer. X-Ray Diffraction (XRD) of the powder samples was obtained using a Philips PW1710 diffractometer equipped with copper anodes. The X-ray source was operated at 40 kV and 40 mA and the 2θ scan was performed in the $10^\circ < 2\theta < 90^\circ$ range each 0.02° and with scan step speed of 1.25s. FTIR spectra of the nanoparticles and ligands were collected on a FTIR-8400S Shimadzu spectrometer in a $4000\text{--}400\text{ cm}^{-1}$ range. Thermogravimetric measurements were performed in a NETZSCH STA 449 C thermogravimetric analyzer, by heating 10 mg of sample at $10^\circ\text{C}/\text{min}$ under dry Ar atmosphere. An additional analysis under air was made in selected samples. TEM micrographs were obtained using a Philips CM200 microscope at an acceleration voltage of 200 kV. For preparing the samples, powders were dispersed in toluene and dropped-cast onto copper grid. EMR spectra were recorded on a Bruker ELESYS spectrometer, equipped with a standard Oxford low-temperature device operating at X band; all measurements were carried out in toluene dispersions and with the same concentration as used in hyperthermia experiments. Magnetic characterization has been performed in powder samples (after precipitating and drying the colloids) and in samples obtained by embedding the colloidal dispersion in polystyrene. The measurements of magnetization versus temperature at 10 Oe were carried out in the temperature range of 5-300 K using a Quantum Design MPMS-7 SQUID magnetometer. Hysteresis loops at room temperature were done in a home-made VSM magnetometer up to a maximum field of 18 kOe with high low field resolution. Hysteresis loops at 5 K were performed in a VSM magnetometer from Cryogenic Ltd up to a maximum field of 100 kOe. Measurements of the Specific Absorption Rate were carried out in a previously described home-made device²⁹ able to operate up to c.a. 1 MHz and with magnetic field amplitudes up to 30 kA/m. The measurements were performed in toluene dispersions of nominally equal concentrations ($\sim 5\text{ mg Fe}_3\text{O}_4/\text{ml}$).

Results and discussion

Basic characterization of the nanoparticles has been done by X-Ray Diffraction (XRD), Infrared Spectroscopy (IR), Thermogravimetric analysis and Transmission Electron Microscopy (TEM). X-ray diffraction, performed in powder samples, show the characteristic pattern of nanocrystalline structures, compatible in all the cases with magnetite (LCPDS N° 19-629), with quite broad diffraction peaks as expected from small crystalline domains (Figure S1 in S.I.). Information about the size of these domains can be achieved by the analysis of the main diffraction peak (311) by the Scherrer's equation (details in Table S2 in S.I.). Figure 1 shows experimental (311) diffraction peaks of samples A and E

together with their deconvolution in order to obtain Bragg position and full width at half maximum (FWHM). Numerical findings of mean sizes are collected in Table 1, where these data are compared with those provided by another two experimental probes, TEM and magnetic measurements.

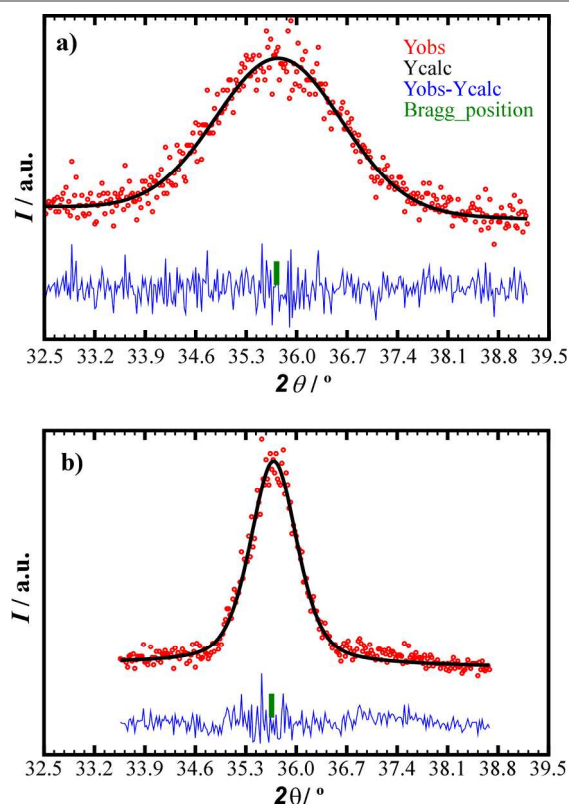


Fig. 1 Deconvolution of experimental (311) diffraction peak of **a)** sample A and **b)** sample E.

Infrared Spectroscopy measurements have been performed both on the pure surfactant agents (oleic acid, 1,2 hexadecanediol and oleylamine) and on magnetite nanoparticles in order to determine the prevailing capping agent and its absorption mechanisms at the particles surface (Figure S2 in S.I.). Infrared spectra demonstrate that the ligand adsorbed in the nanoparticles surface is oleic acid. The C=O stretch band of the carboxyl group, which was detected at 1712 cm^{-1} in pure oleic acid, was absent in the IR spectra of magnetite. Instead, two new bands arise at 1543 and 1628 cm^{-1} , which are characteristic of the asymmetric $\nu_{\text{as}}(\text{COO}^-)$ and the symmetric $\nu_{\text{s}}(\text{COO}^-)$ stretch. This bonding pattern can be explained assuming a combination of molecules bonded symmetrically and forming an angle with the surface of nanoparticles³⁰. Considering also that the absorption at 1053 cm^{-1} arises from C-O single bond stretching, it is clear that oleic acid is chemisorbed onto the Fe_3O_4 nanoparticles as a carboxylate. On the other hand, the two bands placed at 610 and 440 cm^{-1} are the characteristic absorption bands of the Fe-O bond in Fe_3O_4 ³¹.

Thermogravimetric analysis under Ar shows a weight loss between 15 to 37% from bigger to smaller particle size (from E to A), attributed to the oleic acid ligand, and directly related to

the surface area of the NPs. As seen in Figure 2, the decomposition profile consists of different stages: The first loss is originated by solvent remainders in the powder and is located around 100 °C, while the second loss happens between 300 °C and 400 °C and corresponds to organic ligand loss. Subsequently, the reorganization of organic matter forms carbonates which are stabilized from 400 °C until 680 °C, when decompose to form an inorganic residue. The diffraction analysis of this residue is consistent with the presence of Fe₃O₄. In this sense, the weight loss above 100 °C belongs to organic matter and is in good agreement with that observed from chemical analysis. Furthermore, extra thermogravimetric measurements have been performed in air flux in order to confirm the presence of magnetite phase. At around 220 °C it has been observed a weight gain of approximately 3 %, which can be attributed to the oxidation of Fe²⁺ in stoichiometric magnetite to Fe⁺³ to form Fe₂O₃ phase³².

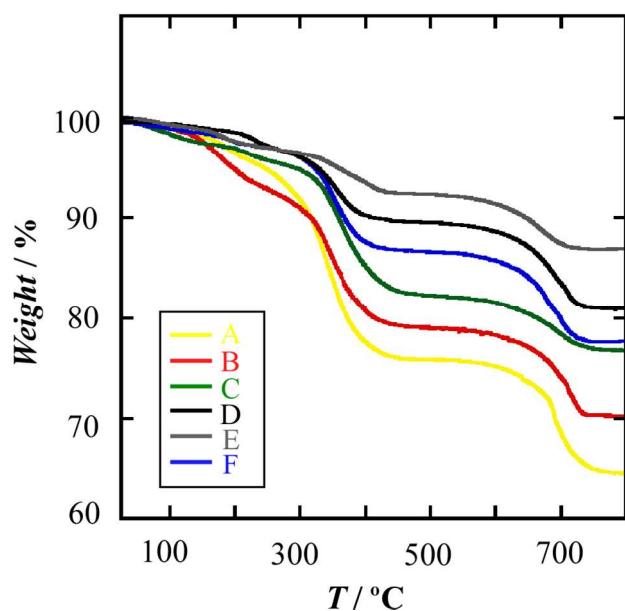


Fig 2. Thermogravimetric measurements in Ar up to 800 °C of samples A-F.

Figure 3 shows TEM images of the final products of samples A-F after the cleaning process. These pictures show a very monodisperse and faceted nanoparticles with a strong tendency to self-assembling (see insets in Figure 3). The size analysis of these images fits to Gaussian profiles, with dispersion indices (β), defined as the ratio of standard deviation to mean diameter, between 0.09 and 0.15 (Table 1). The calculated d-spacings from Electron Diffraction Patterns match well with those corresponding to magnetite (Fe₃O₄)³³. As shown in Table 1, mean sizes derived from TEM are in good accord with those calculated from XRD. This agreement supports the conclusion that these nanoparticles are single crystals, so discarding the appearance of twinning effects, multiple stoichiometry or significant disorder.

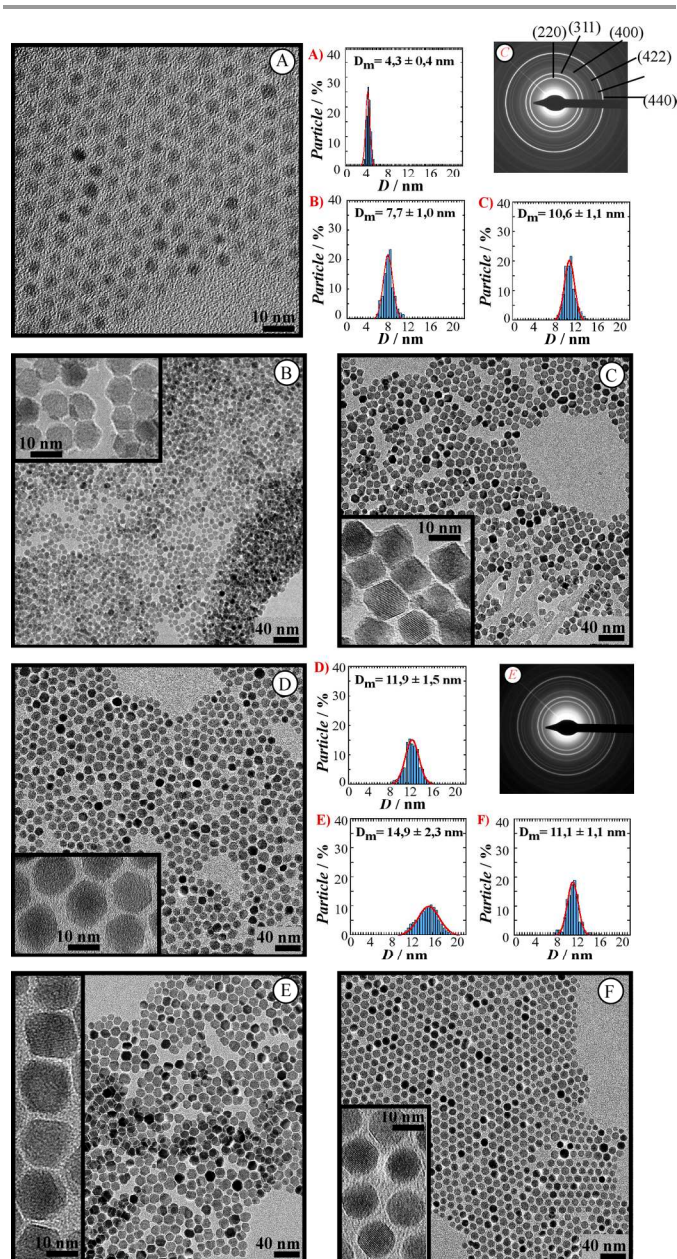


Fig 3. TEM images of samples A-F together with size distributions of the inorganic core and the Electron Diffraction Patterns from selected area of samples C and E.

Table 1. Summary of crystallite sizes obtained by XRD and particle sizes by TEM and magnetic measurements for samples A-F.

Sample Number of additions	D/nm / β TEM	D/nm XRD	D/nm Magnetism
A (1)	4.3±0.4 / 0.09	4.5±0.5	4.2±0.5
B (3)	7.7±1.0 / 0.13	8.0±0.5	7.8±1.4
C (3+1)	10.6±1.1 / 0.10	10.5±0.5	9.5±1.6
D (4)	11.9±1.5 / 0.13	12.0±0.5	11.0±1.8
E (5)	14.9±2.3 / 0.15	14.0±0.5	13.4±2.5
F (5 [*])	11.1±1.1 / 0.10	10.0±0.5	10.4±1.9

*concentration of reagents reduced to half

As mentioned in the introduction seed mediated growth method can lead to multimodal size distribution due to the coexistence of particles in different growing stage. In this way, as-prepared samples were exposed to cleaning cycles, i.e., to a size selective precipitation process with ethanol and toluene in order to reduce the polydispersity. The degree of purity achieved after several cleaning cycles is not easily determined by methods based in microscopic measurements. TEM, for instance, does not always assure the ability to detect the fine details of size distribution.

In this regard, the versatility of EMR to study the fine features of Fe_3O_4 has been demonstrated before^{34,35} and in the present work the use of this technique has been crucial for monitoring the purifying cycles and even for discarding those samples exhibiting too much dispersity. In Figure 4 several room temperature EMR spectra corresponding to consecutive cleaning steps of sample C are presented as illustration. EMR spectrum of the initial product, displayed in the top of Figure 4, shows the existence of various magnetic contributions and some of them disappear after several cleaning processes, as observed when going down to the bottom of Figure 4. This could be explained by the coexistence of NPs with different sizes in the as-prepared sample, considering that the cleaning consists in a size selective precipitation process that allows for the discrimination of NPs around a given size. In this exemplary case, the careful analysis of TEM images was not able to appreciate any change in the size distribution of consecutive cleanings. In contrast, the rather huge (macroscopic) number of analyzed particles by EMR makes this technique a very valuable tool to detect fine changes in sizes which, as will be discussed later, has a measurable impact in the heating ability of colloids in hyperthermia measurements.

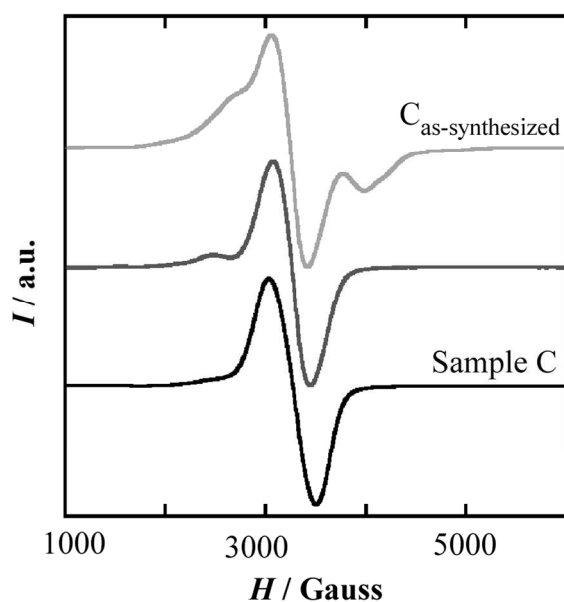


Fig 4. EMR spectra obtained at a frequency of 9.39 GHz for sample C in consecutive cleaning steps.

The distinct resonant lines observed by EMR should be originated by particles of different sizes and/or a diversity of agglomerates. Similar EMR spectra with different magnetic contributions have been previously reported³⁶, and these features were attributed to additional shells originated during the growing process. This explanation would imply that magnetic nanoparticles should not behave as single magnetic domains in the superparamagnetic regime and, consequently, magnetization would not be expected to follow the simple Neel relaxation model under an external applied magnetic field. This multi-shell model does not seem to explain the removal of resonant lines after the cleaning and is hardly compatible neither with magnetization measurements nor with sizes of crystalline domains deduced from XRD analysis.

The effect observed in Figure 4 can be qualitatively explained considering the physical meaning of the position of resonance line (g-factor) in measurements performed in colloids of MNPs. The possible deviation of g-effective (g_{eff}) from 2 does not account for a fundamental change of the internal spin of the particle but it is related to its ability to physically rotate towards the direction of the external applied field when it is in a liquid medium. As a consequence, g_{eff} becomes a measure of the degree of alignment which in turn depends on the internal anisotropy field of nanoparticles ($\sim KV$, where K is the crystal anisotropy constant and V the volume) that increases with the particle size. In this way, particles with similar morphological and magnetic properties but of dissimilar sizes are expected to have different resonance fields. In this framework the small resonant line located at lower field in Figure 4 corresponds indeed to a small percentage of larger particles that have been removed with cleaning.

This approach is also applicable to the analysis of EMR spectra of samples A-F. Figure 5a shows some EMR spectra at room temperature, measured in colloidal medium and corresponding to preparations subjected to a careful size selective cleaning process. The spectra exhibit a unique and well-resolved line that does not depend on the concentration of nanoparticles below a limit of 10 mg/ml, well above the values used in hyperthermia experiments (around 5 mg Fe_3O_4 /ml). At higher concentrations, line-width and resonant field become dependent on the degree of dilution due to the critical increase of interparticle dipolar interactions and/or the onset of strong aggregation effects. The line shape evolves from a nearly-Lorentzian, for sample A, to a Gaussian profile, for the rest, which is a sign of the gradual reinforcement of interparticle interactions when the size or the magnetic moment increases. Samples with a high degree of poly-dispersity give rise to spectra with more than one signal or even very wide lines corresponding to highly broad dispersion of sizes.

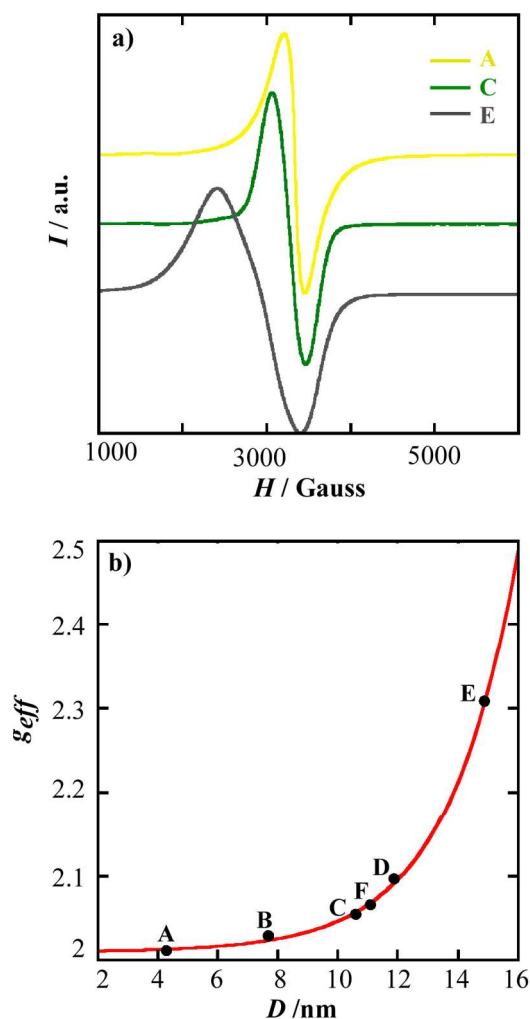


Fig 5. a) Room temperature EMR spectra obtained at a frequency of 9.39 GHz for cleaned samples in toluene dispersion (A, C and E). **b)** Correlation between g_{eff} and mean diameter of nanoparticles.

As expected from previous discussion, nanoparticle size is strongly correlated with g_{eff} that shifts appreciably from 2 for all the samples. The type of correlation is apparent from Figure 5b: g -factor increases sharply with diameter D , in such a way that in the studied range of sizes (4.3 - 14.9 nm) the dependence can be roughly fit to a simple exponential function. Although the theoretical form of this correlation in the whole range of sizes is not expected to follow such simple model, this exponential like correlation, used as a calibration curve, has proved to be quite useful and accurate to estimate sizes, even above the maximum size of sample E. As an example, in Figure 6a it is shown the spectrum of a sample synthesized by the two pot procedure using seeds of 8.5 nm and not belonging to the set of samples A-F. This spectrum is composed of different well-resolved resonant lines revealing the coexistence of the original seeds and new larger particles, namely, a multimodal size distribution. Specifically, up to four contributions are observed, two of them corresponding to very well defined resonance lines. These two lines can be usefully fitted to gaussian functions to determine the corresponding g -factors

(2.08 and 2.59) and, by means of the exponential correlation of Figure 5b, the size of the nanoparticles originating these contributions (11.6 and 16.3 nm, respectively). For this particular case, TEM images also account for the existence of a multimodal distribution of sizes, as observed in Figure 6b. It is very remarkable that sizes calculated by EMR match accurately sizes deduced from TEM, even though one of the populations size is greater than the largest diameter included in the calibration curve of Figure 5b.

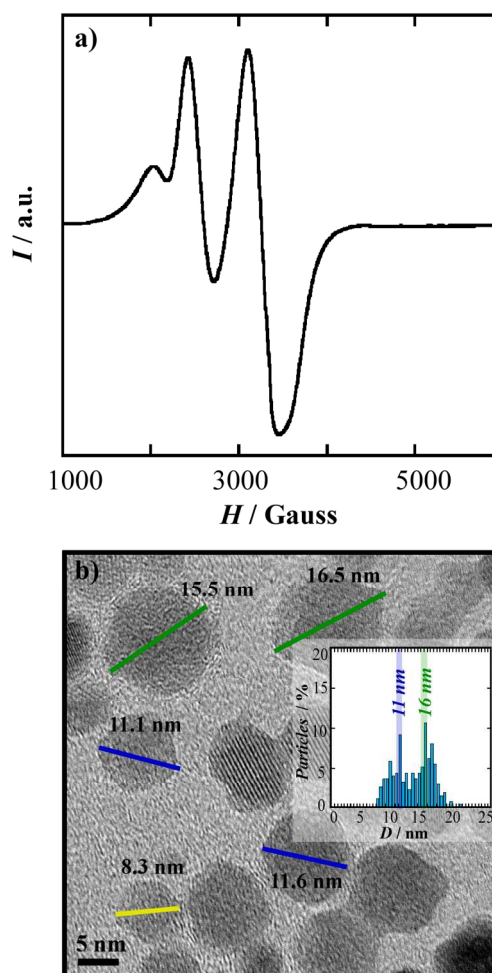


Fig. 6 a) Room temperature EMR spectra obtained at a frequency of 9.39 GHz for as-synthesized sample in a two-pot procedure. **b)** TEM image and size distribution.

It is to note that previous sizes are referred implicitly to the magnetic cores, which in this case correspond to the whole inorganic core of particles. The strong dependence of resonant line position on size above 10 nm also explain the great line broadening and resolution loss of EMR spectra usually observed in samples with a significant degree of size dispersion and/or agglomeration. It is expected the existence of similar correlations in other systems, taking into account their particular characteristics, as liquid medium, morphology, coating, etc. In this way, for a given system the mean size could be predetermined by the g_{eff} from EMR measurements.

The applicability of MNPs for hyperthermia requires a close inspection of their basic magnetic properties that should be well correlated with previous results. This analysis has been performed by macroscopic magnetometry in samples A-F, once the cleaning process was complete. Initial magnetic characterization has been performed in powder samples, after precipitating and drying the colloids. However, samples prepared in this way are not strictly representative of the nanoparticles in the colloidal medium due to the strong agglomeration of particles that brings about intense interparticle interactions. Fine details of the hysteresis loops and magnetization versus temperature curves depend to a great extent on these dipolar interactions (see Figure S3, S4 and S5 in S.I.) and therefore more suitable sample preparation method should be considered. So, the chosen procedure has been to embed the colloidal samples in polystyrene. Measurements of magnetization versus temperature after Cooling at Zero Field (ZFC) and Field (FC) in samples A-F are represented in Figure 7. They show the usual characteristics of a superparamagnetic behaviour, whose most distinctive feature is the increase of the blocking temperature (T_B) with the particle size, from 23 K in the initial seeds, sample A, to 210 K in the largest nanoparticle system, sample E (Table 2). Additionally, dispersion of sizes and, consequently, blocking temperatures originate a broadening of the maximum of the ZFC branch, progressively larger with increasing size because of the strong dependence of T_B on diameter (D), proportional to D^3 in first approximation. Besides, this model does not take into account the interparticle interactions; nevertheless, the dense packing of particles deduced from TEM images in Figure 3 suggests that such interactions are indeed relevant, even in polystyrene dilution. This fact is clearly evident in the FC curves of Figure 7, where the flat response below the maximum in samples D, E and F can be related to the onset of collective blocking of particles³⁷. The effects of interparticle interactions in ZFC-FC curves can be particularly noticed in powder samples where no clear correlation between blocking temperatures and sizes for larger nanoparticles are appreciated (Figure S3 of S.I.).

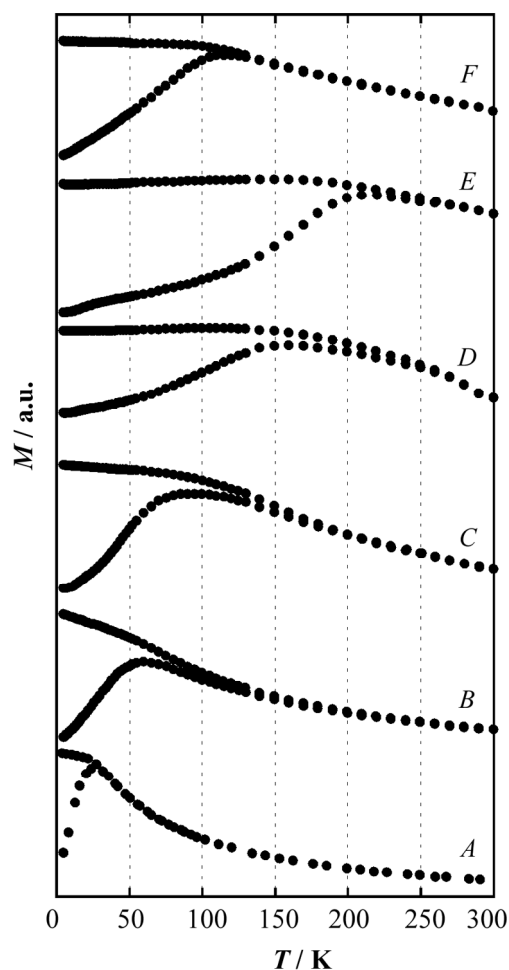


Fig. 7 ZFC/FC curves of sample A-F with an applied field of 10 Oe. They have been obtained from samples in toluene dispersion after embedding them in polystyrene

The superparamagnetic (SPM) character of samples A-F is additionally confirmed by the absence of coercive field (H_C) or remanence (M_r) in the hysteresis loops recorded at room temperature and presented in Figure 8a.

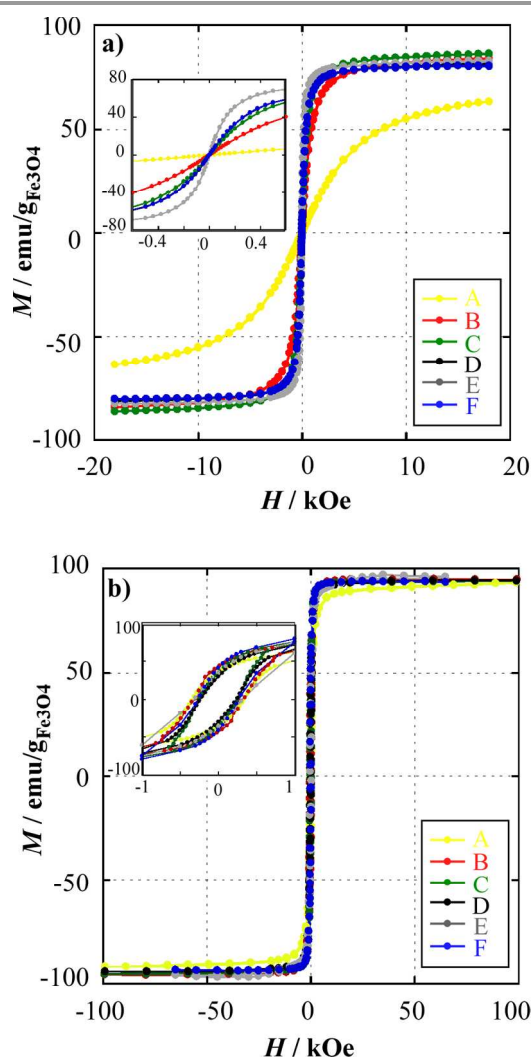


Fig. 8 Hysteresis loops of samples A-F a) at room temperature and b) at 5 K.

Table 2 Summary of magnetic properties for samples A-F.

Sample	$M_S/\text{emu/g}^*$ 5 K	$M_S/\text{emu.g}^{-1*}$ 300 K	T_B/K	H_C/Oe 5K
A	93.3	83.1	23	343
B	97.3	85.6	62	305
C	97.3	86.6	110	257
D	92.1	84.6	160	223
E	97.2	85.2	210	322
F	97.0	84.7	120	265

* M_S values at 300 K and 5 K are taken from measurements in powder up to 100 kOe (see Figure S4 and S5 in S.I.).

The magnetic susceptibility at small enough field of an ideal SPM system is proportional to the particle magnetic moment ($\mu = M_S V$), or assuming a constant spontaneous magnetization (M_S), to the particle volume ($\sim D^3$). This is precisely what is observed in the inset of Figure 8a, where the slope of the $M(H)$ curves close to $H=0$, clearly increases with particle size. A quantitative approach to these curves by using the ideal SPM model³⁸ fits accurately the experimental data, as shown in Figure 9. This model assumes that magnetization verifies the

well-known Langevin function: $M(H) = nM_S L(x)$, where n is the number of particles per unit volume and x is the ratio of magnetic energy (μH) to thermal energy ($k_B T$). In real samples there is an inherent size dispersion that is described by a probability function, $p(D)$. In this way, theoretical $M(H)$ is built as a superposition of a set of Langevin functions, each of which is weighted by its relative probability (see details in Model S1 in S.I.). For this particular case M_S was fixed to the value of bulk magnetite (480 emu/cm^3) being the probability function Gaussian, as deduced from TEM analysis. This calculation provides values (Table 1) for the mean magnetic cores that are in good agreement with particle sizes determined by TEM and XRD. This is particularly true for samples A, B, C and F whose sizes are below 11 nm. The deviation observed in larger particles (samples D and E) could be attributed to dipolar interaction effects, which are strongly sensitive to the total magnetic moment of the particles. Macroscopically such effects can be ascribed to a demagnetizing field which tends to tilt the curve $M(H)$, so hindering the real susceptibility at low fields. This effect becomes indeed stronger in measurements performed in powder samples, where the apparent susceptibility at low field comes to be similar for samples with particles larger than 11 nm (see Figure S4 and S6 in S.I.).

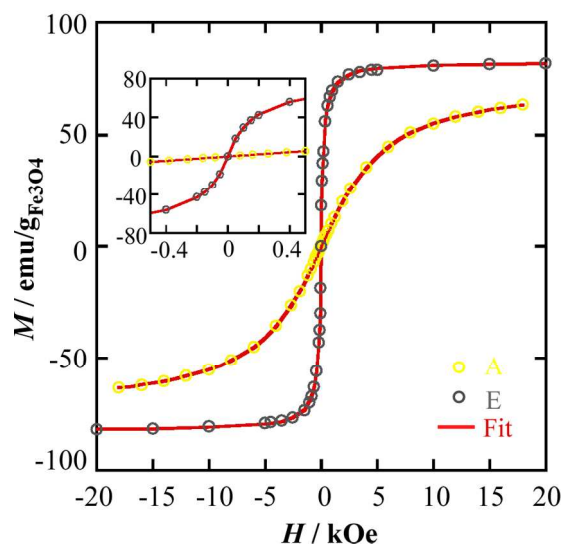


Fig. 9 Fit of $M(H)$ curves at room temperature for samples A and E by SPM model.

Coercive Field (H_C) values observed at 5 K (Table 2) follow basically the expected trend for single magnetic domains: the progressive reduction of the anisotropy constant with size brings about a decrease of H_C , assuming that saturation magnetization is approximately independent of the size. However, this fact does not take into account inter-particle interactions, which could shift the expected H_C to smaller or higher values depending on local ordering of easy axis³⁹. This kind of effects could explain the slightly higher coercive field observed in sample E (322 Oe).

The saturation magnetization values (Table 2) obtained from the hysteresis loops at 5 K (Figure 8b), ranges from 92.1 to 97.3

$\text{emu/g}_{\text{Fe}_3\text{O}_4}$, which agree with the bulk saturation value of magnetite (98 emu/g)⁴⁰. The full saturation at moderate fields ($<5 \text{ kOe}$), is a clear indication of the purity and crystallinity of the samples as well as the minor impact of surface spin disorder on the magnetization process at 5 K ⁴¹. These effects become more visible at room temperature causing a decrease of magnetization to around $85 \text{ emu/g}_{\text{Fe}_3\text{O}_4}$ which is an effect profusely quoted in the literature⁴², and still subjected to discussion. It must be emphasized that the saturation magnetization is a property of utmost importance for the purpose to hyperthermia, and in this sense, values reported in Table 2 confirm that these MNPs meet a priori the first conditions for reaching good levels of power absorption⁴³.

Measurements of Specific Absorption Rate (SAR) as a function of frequency in the range 100-900 kHz with constant AC excitation amplitude of 10 kA/m are presented in Figure 10a. Herein, the experimental trends observed are in good accord with the most distinctive features that could be expected from theory: the nearly linear dependency on frequency at a constant field and, specially, the increase of SAR with size for any frequency in the measured range. Although the close relation of SAR with size has been previously mentioned, a dependency as clear as shown in Figure 10a has not been reported⁴⁴. By plotting the values obtained at 850 kHz (red spots) as a function of size (Figure 10b), a strongly non-linear increase of SAR with size, between $11 \text{ W/g}_{\text{Fe}_3\text{O}_4}$ (sample B) and $414 \text{ W/g}_{\text{Fe}_3\text{O}_4}$ (sample E), is found. It is remarkable that this increase follows quite well the dependence on size predicted by linear response theory⁴⁵. This approach works properly for sufficiently small AC excitation, and thereby some deviation of SAR could be expected for larger particles under an AC field of 10 kA/m ⁴⁶.

The total theoretical SAR model (black line) represented in Figure 10b has been built by convolving the zero dispersity ($\beta=0$) SAR function (grey line) with a Gaussian distribution function of constant dispersity ($\beta=0.15$) that accounts for size dispersity (see details in Model S2 in S.I.). Dispersity (β) has been deduced from TEM values. In calculated SAR, the dependence on size of the anisotropy constant (K), because of the reduction of surface contributions, has been introduced by using a phenomenological approach widely used in previous studies⁴⁷: the effective anisotropy constant (K) is the result of the addition of a volume (K_V) and a surface contribution (K_S) as $K=K_V+K_S*6/D$, where K_V is the anisotropy in the limit of bulk single crystal (11 kJ/m^3 ⁴⁰) and K_S is fixed to $15 \text{ }\mu\text{J/m}^2$ ⁴⁸. As outlined before, there is a good agreement between experimental and calculated SAR upon including the dispersity of sizes (grey line in Figure 10b).

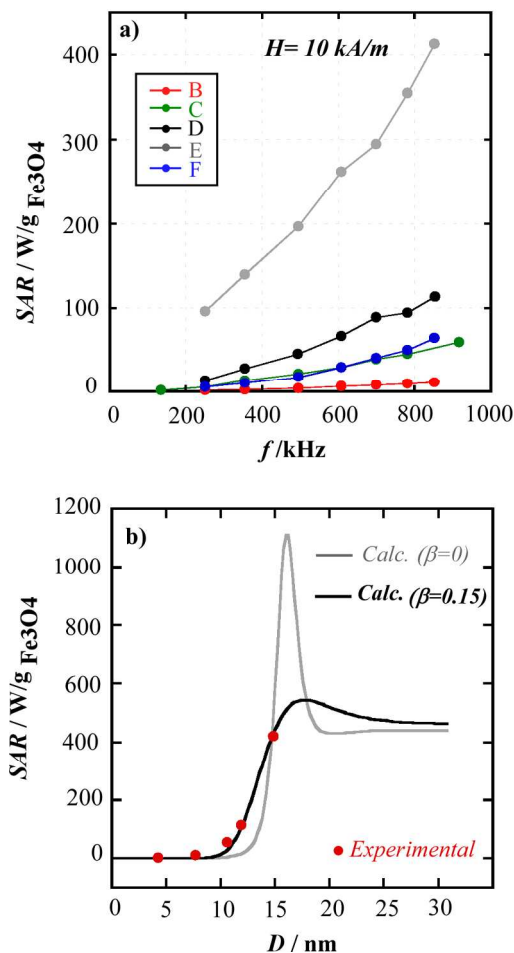


Fig. 10 a) SAR as a function of frequency for samples B-F under an AC field of 10 kA/m . **b)** Calculated SAR as a function of diameter under an AC field of 10 kA/m and a frequency of 850 kHz and experimental values of samples A-E in the same conditions.

The expected impact of size dispersity of a sample in its specific power absorption becomes quite apparent from the Figure 10b and has been discussed before in the literature⁴⁹. This influence is especially marked close to the maximum predicted SAR under a given AC excitation. The size dispersity, intrinsic to any preparation, smoothes the resonant peak, and the higher the dispersity is, the flatter the maximum becomes. Additional experimental confirmation of this fact can be deduced from SAR measurements performed in as-prepared samples before cleaning: SAR obtained at 850 kHz and 10 kA/m in as-synthesized sample E is around $310 \text{ W/g}_{\text{Fe}_3\text{O}_4}$, approximately 25% less than that attained after cleaning ($415 \text{ W/g}_{\text{Fe}_3\text{O}_4}$), (Figure S7 in S.I.). Finally, in Figure 11, the Specific Absorption Rate (SAR) is plotted against the effective g-factor. The linear relation observed between both variables in this particular size range would suggest that a function similar to theoretical SAR could also describe the g_{eff} dependency on size. Moreover, this proportionality would probably works well for samples with small size dispersity in a particular colloidal medium. Thus,

from a practical point of view, the linear correlation represented in Figure 11 implies that EMR technique can be used to estimate directly in a fast and easy way the Specific Absorption Rate of a sample.

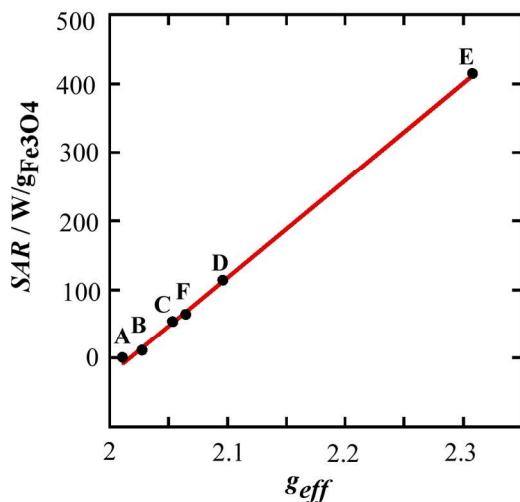


Fig. 11 Linear relation between SAR and g_{eff} values.

Conclusions

Monodisperse Fe₃O₄ nanoparticles have been synthesized by a thermal decomposition method based on consecutive addition steps of iron precursor and ligands, achieving size tunable nanoparticles with high crystallinity and high saturation magnetization. Seed mediated growth has proved to be a very efficient synthetic route to produce high performance nanoparticles for hyperthermia, provided that the magnetic properties of the starting seeds are the best possible. Some details of the synthesis seems to play an essential role for its success: a precise control of relative concentration of surfactants (oleic acid, 1,2-hexadecanediol and oleylamine) and small enough oxygen content in the reaction vessel for preventing the formation of non magnetic layers around the magnetic cores during the subsequent growing steps. It has been found an entire agreement among the size of the nanoparticles determined by TEM, by the deconvolution of the most intense diffraction peak of Fe₃O₄ and by fitting M vs H curves by SPM model. The correlation existing between Specific Absorption Rate and size has been clearly demonstrated empirically. EMR spectroscopy has been shown as a powerful tool to evaluate magnetic size distributions of MNPs in samples with at least 10¹⁴ NPs, corresponding to a standard EMR experiment at room temperature, almost exactly in the same preparation and with the same concentration as used in hyperthermia experiments, allowing also an estimation of the heating power of the samples. In this sense, it also becomes a potent complementary tool of TEM to better fix the features of size distribution. Another particular benefit of this type of experiment arises from its magnetic specificity, in such a way that it could be directly applied to size determination of

MNPs in a physiological environment without any interference from non-magnetic biological components.

Both the developed synthesis protocol and the use of EMR for size determination of MNPs in samples of several milligrams could yield the future opportunity of growing very specific size nanoparticles in a biocompatible medium. The development of this approach would significantly contribute to the field of the magnetic hyperthermia.

Acknowledgment

This work was supported by institutional funding from the Ministerio de Educacion y Ciencia and Basque Government under Projects MAT2010-19942, GIC-IT-570-13 and S-PC11BF004. Dr. I. Castellanos-Rubio thanks the Basque Government for a predoctoral fellowship. We are grateful to Dr. I. Orue for helpful discussion on magnetic properties. Technical and human support provided by SGiker (UPV/EHU) is also gratefully acknowledged.

Notes and references

^aDpto. de Química Inorgánica, Universidad del País Vasco, UPV/EHU, P.O. Box. 644, E-48080, Bilbao, Spain.

^bBCMaterials, Parque Científico y Tecnológico de Bizkaia, E-48160, Derio, Spain.

^cDpto. Electricidad y Electrónica. Universidad del País Vasco, UPV/EHU, P.O. Box. 644, E-48080, Bilbao, Spain.

† **Supporting Information.** Synthetic parameters of Fe₃O₄ nanoparticles obtained by seeded growth method. Diffractograms of samples A-F. Deconvolution from (311) diffraction peak of samples A-F. FTIR spectra of pure oleic acid and Fe₃O₄ nanoparticles coated with oleic acid. ZFC/FC curves of samples A-E in powder. Hysteresis loops of powder samples. Non-Interacting SuperParamagnetic (SPM) model. Fit of M(H) curves at room temperature. Calculation of SAR as a function of particle diameter. SAR values of sample E before and after washing process. This material is available free of charge via the Internet at <http://pubs.acs.org>.

See DOI: 10.1039/b000000x/

- 1 C. Martinez-Boubeta, L. Balcells, R. Cristòfol, C. Sanfeliu, E. Rodríguez, R. Weissleder, S. Lope-Piedrafita, K. Simeonidis, M. Angelakeris and F. Sandiumenge, *Nanomedicine*, 2010, **6**, 362.
- 2 M. Domenech, I. Marrero-Berrios, M. Torres-Lugo and C. Rinaldi, *ACS Nano* 2013, **7**, 5091.
- 3 K. Hayashi, K. Ono, H. Suzuki, M. Sawada, M. Moriya, W. Sakamoto and T. Yogo, *Chem. Mater.*, 2010, **22**, 3768.
- 4 L. Lartigue, C. Innocenti, T. Kalaivani, A. Awwad, M. D. M. Sanchez Duque, Y. Guari, J. Larionova, C. Guérin, J. L. G. Montero, V. Barragan-Montero, P. Arosio, A. Lascialfari, D. Gatteschi and C. Sangregorio, *J. Am. Chem. Soc.*, 2011, **133**, 10459.
- 5 S. Jiang, A. A. Eltoukhy, K. T. Love, R. Langer and D. G. Anderson, *Nano Lett.*, 2013, **13**, 1059.
- 6 P. Wust, B. Hildebrandt, G. Sreenivasa, B. Rau, J. Gellermann, H. Riess, R. Felix and P. M. Schlag, *Lancet Oncol.*, 2002, **3**, 487.
- 7 A. P. Khandhar, R. M. Ferguson, J. A. Simon and K. M. Krishnan, *J. Biomed. Mater. Res., A* 2012, **100**, 728.

- 8 J. P. Fortin, C. Wilhelm, J. Servais, C. Ménager, J. C. Bacri and F. Gazeau, *J. Am. Chem. Soc.*, 2007, **129**, 2628.
- 9 A. Meffre, B. Mehdaoui, V. Kelsen, P. F. Fazzini, J. Carrey, S. Lachaize, M. Respaud and B. Chaudret, *Nano Lett.*, 2012, **12**, 4722.
- 10 B. Qi, L. Ye, R. Stone, C. Dennis, T. M. Crawford and O.T. Mefford, *J. Phys. Chem., C* 2013, **117**, 5429.
- 11 S. H. Gage, B. D. Stein, L. Z. Nikoshvili, V. G. Matveeva, M. G. Sulman, E. M. Sulman, D. G. Morgan, E. Y. Yuzik-Klimova, W. E. Mahmoud and L. M. Bronstein, *Langmuir*, 2013, **29**, 466.
- 12 J. Lee, S. Zhang and S. Sun, *Chem. Mater.*, 2013, **25**, 1293.
- 13 T. Pellegrino, L. Manna, S. Kudera, T. Liedl, D. Koktysh, A. L. Rogach, S. Keller, J. Ra, G. Natile and W. J. Parak, *Nano Lett.*, 2004, **4**, 703.
- 14 S. Sun and H. Zeng, *J. Am. Chem. Soc.*, 2002, **124**, 8204.
- 15 V. F. Puentes, K. M. Krishnan and A. P. Alivisatos, *Science*, 2001, **291**, 2115.
- 16 L. E. Euliss, S. G. Grancharov, S. O'Brien, T. J. Deming, G. D. Stucky, C. B. Murray and G. A. Held, *Nano Letters*, 2003, **3**, 1489.
- 17 D. Portet, B. Denizot, E. Rump, J. J. Lejeune and P. Jallet, *J. Colloid Interf. Sci.*, 2001, **238**, 37.
- 18 P. Guardia, R. Di Corato, L. Lartigue, C. Wilhelm, A. Espinosa, M. García-Hernández, F. Gazeau, L. Manna, T. Pellegrino, *ACS Nano*, 2012, **6**, 3080.
- 19 M. Levy, A. Quarta, A. Espinosa, A. Figuerola, C. Wilhelm, M. García-Hernández, A. Genovese, A. Falqui, D. Alloyeau, R. Buonsanti, P. D. Cozzoli, M. A. García, F. Gazeau and T. Pellegrino, *Chem. Mater.*, 2011, **23**, 4170.
- 20 N. Noginova, T. Weaver, E. Giannelis, A. Bourlinos, V. Atsarkin and V. Demidov, *Phys. Rev. B*, 2008, **77**, 014403.
- 21 M. Yulikov, P. Lueders, M. F. Warsi, V. Chechik and G. Jeschke, *Phys. Chem. Chem. Phys.* 2012, **14**, 10732.
- 22 D. Gatteschi, M. Fittipaldi, C. Sangregorio and L. Sorace, *Angew. Chem.*, 2012, **51**, 4792.
- 23 M. Fittipaldi, L. Sorace, A. L. Barra, C. Sangregorio, R. Sessoli and D. Gatteschi, *Phys. Chem. Chem. Phys.*, 2009, **11**, 6555.
- 24 S. Peng, C. Wang, J. Xie and S. Sun, *J. Am. Chem. Soc.*, 2006, **128**, 10676.
- 25 J. Park, E. Lee, N. M. Hwang, M. Kang, S. C. Kim, Y. Hwang, J. G. Park, N. J. Noh, J. Y. Kim, J. H. Park and T. Hyeon, *Angew. Chem.*, 2005, **44**, 2873.
- 26 A. Cabot, V. F. Puentes, E. Shevchenko, Y. Yin, L. Balcells, M. Marcus, S. M. Hughes, A. P. Alivisatos, *J. Am. Chem. Soc.*, 2007, **129**, 10358.
- 27 H. Lee, T. J. Yoon and R. Weissleder, *Angew. Chem.*, 2009, **48**, 5657.
- 28 C. A. J. Lin, R. Sperling, J. K. Li, T. Y. Yang, P. Y. Li, M. Zanella, W. H. Chang and W. J. Parak, *Small*, 2008, **4**, 334.
- 29 F. Plazaola, E. Garaio, J. M. Collantes, I. Castellanos, M. Insausti, I. Gil de Muro and J. A. Garcia, *J. Nanosci. Nanotechnol.*, 2012, **12**, 7451.
- 30 Y. T. Tao, *J. Am. Chem. Soc.*, 1993, **115**, 4350
- 31 M. Ma, Y. Zhang, W. Yu, H. Shen, H. Zhang and N. Gu, *Colloids and Surfaces A*, 2003, **212**, 219.
- 32 F. Dang, N. Enomoto, J. Hojo and K. Enpuku, *Ultrason Sonochem.*, 2009, **16**, 649.
- 33 W. W. Yu, J. C. Falkner, C. T. Yavuz and V. L. Colvin, *Chem. Commun.*, 2004, 2306.
- 34 P. Ceci, E. Chiancone, O. Kasyutich, G. Bellapadrona, L. Castelli, M. Fittipaldi, D. Gatteschi, C. Innocenti and C. Sangregorio, *Chem. Eur. J.*, 2010, **16**, 709.
- 35 J. Salado, M. Insausti, L. Lezama, I. Gil de Muro, E. Goikolea and T. Rojo, *Chem. Mater.*, 2011, **23**, 2879.
- 36 L. Lartigue, P. Hugounenq, D. Alloyeau, S. P. Clarke, M. Lévy, J. C. Bacri, R. Bazzi, D. F. Brougham, C. Wilhelm and F. Gazeau, *ACS Nano*, 2012, **6**, 10935.
- 37 J. Vargas, W. Nunes, L. Socolovsky, M. Knobel and D. Zanchet, *Phys. Rev. B*, 2005, **72**, 184428.
- 38 M. Knobel, W. C. Nunes, L. M. Socolovsky, E. De Biasi, J. M. Vargas and J. C. Denardin, *J. Nanosci. Nanotechnol.*, 2008, **8**, 2836.
- 39 X. Batlle and A. Labarta, *J. Phys. D: Appl. Phys.*, 2002, **35**, R15.
- 40 B. Cullity, *Introduction to Magnetic Materials*, Addison-Wesley, Massachusetts, USA, 1972, 190.
- 41 X. Batlle, N. Pérez, P. Guardia, O. Iglesias, A. Labarta, F. Bartolomé, L. M. García, J. Bartolomé, A. G. Roca, M. P. Morales and C. J. Serna, *J. Appl. Phys.*, 2011, **109**, 07B524.
- 42 K. Mandal, S. Mitra and P. A. Kumar, *Europhys. Lett.*, 2006, **75**, 618.
- 43 K. Hayashi, M. Moriya, W. Sakamoto and T. Yogo, *Chem. Mater.*, 2009, **21**, 1318.
- 44 R. Chen, M. G. Christiansen and P. Anikeeva, *ACS Nano*, 2013, **7**, 8990.
- 45 J. P. Fortin, F. Gazeau, C. Wilhelm, *Eur. Biophys. J.* 2008, **37**, 223.
- 46 E. L. Verde, G. T. Landi, J. A. Gomes, M. H. Sousa, A. F. Bakuzis, *J. Appl. Phys.* 2012, **111**, 123902.
- 47 F. Luis, J. Torres, L. García, J. Bartolomé, J. Stankiewicz, F. Petroff, F. Fetta, J. L. Maurice and A. Vaurès, *Phys. Rev. B* 2002, **65**, 094409.
- 48 M. Thakur, K. De, S. Giri, S. Si, A. Kotal and T. K. Mandal, *J. Phys: Condens Matter*, 2006, **18**, 9093. M. Thakur, K. De, S. Giri, S. Si, A. Kotal and T. K. Mandal, *J. Phys: Condens Matter*, 2008, **20**, 149801.
- 49 M. B. Fernández van Raap, P. Mendoza Zélis, D. F. Coral, T. E. Torres, C. Marquina, Goya and F. H. Sánchez, *J. Nanopart., Res.* 2012, **14**, 1072.